

Table 2. Cox proportion hazards model for RFS and OS ($n = 110$)

Variable	Univariate		Multivariate	
	HR (95% CI)	P	HR (95% CI)	P
RFS				
Age (≥ 70 vs. <70)	1.49 (0.71–3.17)	0.296		
Sex (male vs. female)	2.30 (1.09–5.06)	0.029	2.49 (1.13–5.74)	0.024
Smoking (current or former vs. never)	1.05 (0.49–2.21)	0.907		
<i>EGFR</i> mutation (positive vs. negative)	0.72 (0.32–1.51)	0.382		
Aromatase (high vs. low)	3.01 (1.35–6.64)	0.008	2.37 (1.05–5.31)	0.039
Pathologic stage (\geq II vs. I)	5.33 (2.53–11.5)	<0.001	3.36 (1.50–7.70)	0.003
OS				
Age (≥ 70 vs. <70)	2.85 (1.06–8.97)	0.041		
Sex (male vs. female)	2.74 (1.04–7.97)	0.038		
Smoking (current or former vs. never)	0.76 (0.28–1.98)	0.573		
<i>EGFR</i> mutation (positive vs. negative)	0.25 (0.06–0.78)	0.015		
Aromatase (high vs. low)	4.20 (1.49–12.1)	0.007		
Pathologic stage (\geq II vs. I)	3.54 (1.35–9.46)	0.011		

NOTE: Multivariate analysis for OS was not performed because of the small number of events (deaths).

expressing cell line and HCC4006 as low-aromatase mRNA-expressing cell line, both of which have *EGFR* mutations. To test the growth inhibitory effects of the aromatase inhibitor exemestane, we conducted an MTT assay. HCC4006 was not sensitive to exemestane, either alone or combined with erlotinib (Fig. 3B). By contrast, 11-18 was sensitive to exemestane alone (Fig. 3C), and its cell growth was significantly inhibited by the combination of exemestane with erlotinib. We further tested the growth inhibitory effects of exemestane in high-aromatase mRNA-expressing cell lines without *EGFR* mutations: H358 (Supplementary Fig. S2A), H2228 (Supplementary Fig. S2B), and ACC-LC-319 (Supplementary Fig. S2C). The antitumor effect of exemestane in H358, H2228, and ACC-LC-319 was much weaker than in 11-18.

Discussion

Although increasing evidence indicates that female hormones affect development of lung cancer (34–36), to our knowledge, this study is the first report to elucidate the prognostic significance of aromatase expression in patients

with lung adenocarcinomas with *EGFR* mutations. We found that aromatase mRNA expression level was not correlated with clinicopathologic factors, including *EGFR* mutation status. However, high aromatase expression was associated with poor prognosis in terms of both RFS and OS. Moreover, the prognostic significance of aromatase expression was limited to females, never-smokers, and patients with *EGFR* mutations, whereas such significance was not observed in their counterparts.

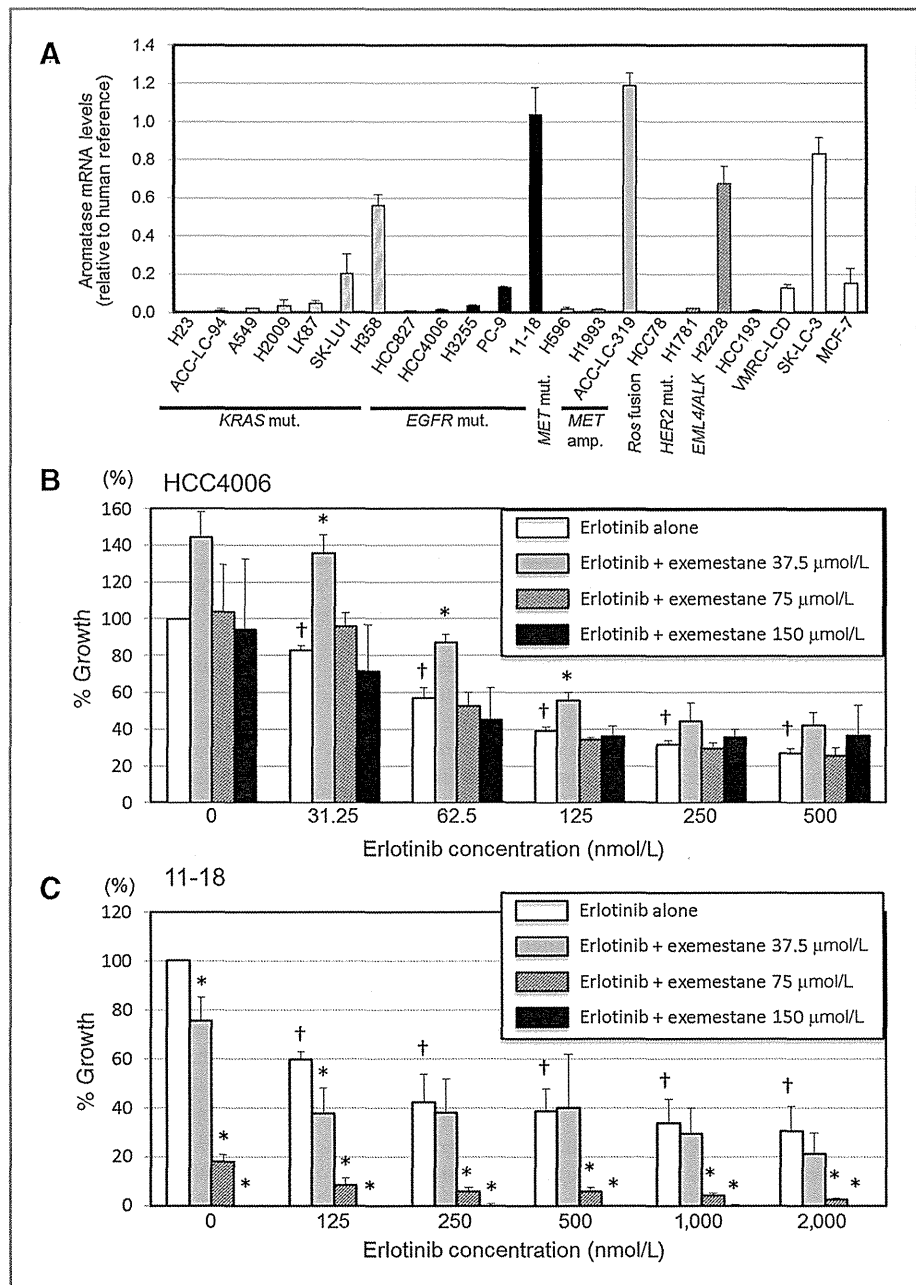
Aromatase is an enzyme that catalyzes the conversion from androgens to estrogens. In NSCLC cells, estrogen is reported to be mainly produced by intrinsic aromatase (23), and stimulates the ER signaling pathway, resulting in tumor development and progression (9–11, 13, 24). Here, we found that aromatase mRNA expression levels in carcinoma tissues were significantly higher than in corresponding nonneoplastic lung tissues. Niikawa and colleagues reported that the estradiol concentration in NSCLC was significantly higher than that in the nonneoplastic lung tissues, and intratumoral estradiol concentration in NSCLC was positively associated with aromatase mRNA expression

Table 3. Cox proportion hazards model for RFS in patients with *EGFR* mutations ($n = 54$)

Variable	Univariate	
	HR (95% CI)	P
Age: ≥ 70 ($n = 21$) vs. <70 ($n = 33$)	0.85 (0.22–2.82)	0.795
Sex: male ($n = 12$) vs. female ($n = 42$)	3.48 (0.99–11.6)	0.050
Smoking: current/former ($n = 15$) vs. never ($n = 39$)	1.60 (0.42–5.30)	0.466
Aromatase: high ($n = 15$) vs. low ($n = 39$)	4.97 (1.50–19.0)	0.009
Pathologic stage: \geq II ($n = 13$) vs. I ($n = 41$)	6.55 (1.98–25.0)	0.002

NOTE: Multivariate analysis was not performed because of the small number of recurrences.

Figure 3. Effect of exemestane alone and in combination with erlotinib on *EGFR* mutant lung adenocarcinoma cell line proliferation. **A**, mRNA expression levels of aromatase in 21 human lung adenocarcinoma cell lines. Quantitative real-time RT-PCR was performed with validated TaqMan probes; assays were done in triplicate. The expression value for each cell line was calculated relative to that of human reference. MCF-7: breast carcinoma cell line. **B**, HCC4006 cells were not sensitive to exemestane alone or in combination with erlotinib. **C**, 11-18 cells were sensitive to exemestane alone and in combination with erlotinib. HCC4006 and 11-18 cells were incubated for 24 hours and for an additional 72 hours with the indicated concentrations of exemestane or erlotinib; cell growth was then measured. Independent experiments were repeated 3 times. *, $P < 0.05$ vs. erlotinib alone; †, $P < 0.05$ vs. control (both erlotinib and exemestane were free) by Dunnett test. All data represent the mean \pm SD from 3 independent experiments.



(23). In another study, levels of aromatase activity tested by radioassay were significantly greater in tumors compared with those in nearby normal tissue (12). These studies indicate that intrinsic aromatase expression levels are closely associated with the estrogen levels in the lung cancer cells. Thus, increased aromatase level may have profound influence in carcinoma tissues through estrogen function.

Most estrogenic actions are mediated by ER, which exists in 2 forms, ER α and ER β (37). Although immunohistochemical expressions of ER α and/or ER β has been associated with clinical outcome in some studies (14–16, 26, 38),

the findings for expression frequency and subcellular localization (nuclear or cytoplasm) of ERs are inconsistent (14–16, 27, 36, 38, 39). These differences could be because of variation in such factors as (a) antibodies and dilutions, (b) scoring systems for staining, and (c) patient cohort characteristics (16). This discrepancy may obscure the significance of hormone receptor expression in patients' clinicopathologic characteristics or prognoses. For this reason, we found it difficult to clarify the effect of estrogen on the development of lung cancer using immunohistochemical analysis.

In this study, no significant correlation was identified between tumor aromatase expression and clinicopathologic factors, including *EGFR* mutations, when analyzed as either dichotomized or continuous variables. These results are consistent with previously reports (27, 39, 40). However, a correlation between *EGFR* mutation and ER expression, both ER α (14) and nuclear ER β (15), in lung adenocarcinoma, was reported in previous studies, suggesting that some interaction between ER and the *EGFR* signaling pathway may exist.

High aromatase expression was associated with a poor prognosis in patients who underwent curative resections for lung adenocarcinoma. We also demonstrated that the prognostic significance of aromatase expression was limited to females, never-smokers, and patients with *EGFR* mutations, whereas such significance was not observed in their counterparts. We conducted Cox proportional hazards analysis in patients with *EGFR* mutations by RFS, not by OS, because 8 of 11 patients (73%) with *EGFR* mutations had received *EGFR*-TKI treatment for recurrence. *EGFR*-TKI prolonged the survival of such patients; therefore, the follow-up period may not have been enough to evaluate OS in this study. Aromatase expression level and *EGFR* mutation status did not directly correlate, but aromatase expression only held prognostic significance for lung adenocarcinomas with *EGFR* mutations, which suggests that estrogenic signaling augments growth that depends on the *EGFR* pathway. Mah and colleagues reported that lower aromatase levels predicted greater chances of survival in women 65 years and older with NSCLC, particularly among women who had no smoking history (13). Although they did not investigate *EGFR* mutation status, their results are consistent with ours. Nose and colleagues reported that strong nuclear expression of ER β correlated with better disease-free survival in patients with *EGFR* mutations, but found no such prognostic significance in patients without *EGFR* mutations (15). They also suggested that strong ER β expression was a surrogate marker for good response to *EGFR*-TKI (26). These results, along with our own, indicate that female hormone-related factors, such as aromatase and ER β , affect outcomes only in lung adenocarcinomas with *EGFR* mutation, which suggests that hormonal and *EGFR* pathways may contribute in concert to progression of lung adenocarcinoma.

To investigate the influence of differences in aromatase expression between the tumor and normal tissues on patient survival, we classified patients into the following 2 groups: T > N, in whom aromatase expression in adenocarcinoma tissue was higher than in nonneoplastic lung tissue ($n = 51$); and T < N, in whom it was lower ($n = 43$). We performed survival analyses between the 2 groups, but saw no significant survival difference in RFS ($P = 0.22$) or OS ($P = 0.27$). We further compared RFS and OS between the 2 groups in subsets divided by sex, smoking history, and *EGFR* mutation status, but saw no significant difference in these analyses (data not shown).

Recently, interactions between the ER and *EGFR* pathways have been investigated *in vitro*. A nonnuclear ER pool

has been proposed that works via rapid signaling through various kinase cascades, including *EGFR* pathway and its downstream effectors in the lungs, such as MAPK (10, 11). However, the ER and *EGFR* pathways seem to act as alternate signaling pathways, with one upregulating when the other is inactivated (10, 41). This bi-directional crosstalk between ER and *EGFR* signaling suggests that simultaneous or combined therapy that targets both pathways could exert higher antitumor effect in patients with NSCLC.

Both *in vitro* and *in vivo* reports have demonstrated that estrogen downmodulator, alone or combined with *EGFR*-TKI, resulted in enhanced antitumor activity in NSCLCs (9–12, 23, 25, 41–44). Exemestane, an irreversible steroidal inactivator, either alone (41) or in combination with cisplatin (43) showed significant antitumor effects in 2 separate studies. Both letrozole and anastrozole, reversible steroidal inactivators, demonstrated similar antitumor activity in NSCLCs (12, 23, 44). However, lung cancer cell lines used in almost all of these studies were without *EGFR* mutations. We showed that the 11-18 cell line, which has an *EGFR* mutation accompanied with a high aromatase mRNA expression, was sensitive to exemestane alone and cell growth was significantly inhibited by the combination of exemestane and erlotinib. We also demonstrated that exemestane's antitumor effects in H358, H2228, and ACC-LC-319, which have high aromatase expressions without *EGFR* mutations, were much weaker than in 11-18. These results suggest that sensitivity to the aromatase inhibitor may depend on crosstalk between ER and the *EGFR* pathway; reducing estrogenic signaling by inhibiting aromatase might inhibit cell growth that depends on the *EGFR* pathway. Therefore, our result suggests that selecting patients with high aromatase expression accompanied by *EGFR* mutation might improve clinical responses to the combination of *EGFR*-TKI and aromatase inhibitor. However, we tested the growth inhibitory effects of only one cell line with high aromatase expression and *EGFR* mutation, thus this study remains limited. Further studies using *in vivo* and clinical models are needed to elucidate the therapeutic potential of aromatase inhibitor in lung adenocarcinomas with *EGFR* mutations. Traynor and colleagues reported a pilot study of gefitinib and fulvestrant in the treatment of 22 postmenopausal women diagnosed as NSCLC (45). No significant results were obtained in this small study, but combination therapy was well tolerated. Three of 12 patients tested for *EGFR* mutation status detected *EGFR* mutation. A trial of *EGFR*-TKI and estrogen downmodulator in patients with NSCLC with *EGFR* mutations may be therefore needed in the future.

In conclusion, high aromatase expression is correlated with poor outcome in patients with lung adenocarcinoma, including those with *EGFR* mutations. Aromatase may be a useful therapeutic target in lung adenocarcinomas with high aromatase expression and *EGFR* mutations. Although our results provide potential insights into the influence of aromatase expression in lung cancer, further studies are required to better understand the

mechanisms of aromatase expression and interaction with *EGFR* signaling, and to determine the clinical applicability of aromatase inhibitors.

Disclosure of Potential Conflicts of Interest

Y. Maehara reports receiving other research grants from Chugai and Pfizer. No potential conflicts of interest were disclosed by the other authors.

Authors' Contributions

Conception and design: M. Kohno, T. Okamoto, K. Suda
Development of methodology: M. Kohno, K. Suda, T. Yano
Acquisition of data (provided animals, acquired and managed patients, provided facilities, etc.): M. Kohno, T. Yano
Analysis and interpretation of data (e.g., statistical analysis, biostatistics, computational analysis): M. Kohno, K. Suda, M. Shimokawa
Writing, review, and/or revision of the manuscript: M. Kohno, T. Okamoto, M. Shimokawa, M. Takenoyama, T. Yano

Administrative, technical, or material support (i.e., reporting or organizing data, constructing databases): K. Suda, H. Kitahara, S. Shimamatsu, H. Konishi, T. Yoshida

Study supervision: M. Takenoyama, T. Yano, Y. Maehara

Acknowledgments

The authors thank Dr. A.F. Gazdar, Dr. T. Hida, Dr. K. Tomizawa, Dr. T. Mitsudomi, and Dr. M. Takeshita for kindly providing cell lines.

Grant Support

This study was supported in part by a Grant-in-Aid for Scientific Research (C) from the Japan Society for the Promotion of Science (21591816).

The costs of publication of this article were defrayed in part by the payment of page charges. This article must therefore be hereby marked *advertisement* in accordance with 18 U.S.C. Section 1734 solely to indicate this fact.

Received September 30, 2013; revised April 13, 2014; accepted April 14, 2014; published OnlineFirst May 6, 2014.

References

- Jemal A, Bray F, Center MM, Ferlay J, Ward E, Forman D. Global cancer statistics. *CA Cancer J Clin* 2011;61:69–90.
- Sun S, Schiller JH, Gazdar AF. Lung cancer in never smokers—a different disease. *Nat Rev Cancer* 2007;7:778–90.
- Yano T, Miura N, Takenaka T, Haro A, Okazaki H, Ohba T, et al. Never-smoking nonsmall cell lung cancer as a separate entity: clinicopathologic features and survival. *Cancer* 2008;113:1012–8.
- Yano T, Haro A, Shikada Y, Maruyama R, Maehara Y. Non-small cell lung cancer in never smokers as a representative 'non-smoking-associated lung cancer': epidemiology and clinical features. *Int J Clin Oncol* 2011;16:287–93.
- Shigematsu H, Lin L, Takahashi T, Nomura M, Suzuki M, Wistuba II, et al. Clinical and biological features associated with epidermal growth factor receptor gene mutations in lung cancers. *J Natl Cancer Inst* 2005;97:339–46.
- Kosaka T, Yatabe Y, Endoh H, Kuwano H, Takahashi T, Mitsudomi T. Mutations of the epidermal growth factor receptor gene in lung cancer: biological and clinical implications. *Cancer Res* 2004;64:8919–23.
- Shaw AT, Yeap BY, Mino-Kenudson M, Digumarthy SR, Costa DB, Heist RS. Clinical features and outcome of patients with non-small-cell lung cancer who harbor *EML4-ALK*. *J Clin Oncol* 2009;27:4247–53.
- Patrone C, Cassel TN, Petterson K, Piao YS, Cheng G, Ciana P, et al. Regulation of postnatal lung development and homeostasis by estrogen receptor β . *Mol Cell Biol* 2003;23:8542–52.
- Stabile LP, Davis AL, Gubish CT, Hopkins TM, Luketich JD, Christie N, et al. Human non-small cell lung tumors and cells derived from normal lung express both estrogen receptor α and β and show biological responses to estrogen. *Cancer Res* 2002;62:2141–50.
- Stabile LP, Lyker JS, Gubish CT, Zhang W, Grandis JR, Siegfried JM. Combined targeting of the estrogen receptor and the epidermal growth factor receptor in non-small cell lung cancer shows enhanced anti-proliferative effects. *Cancer Res* 2005;65:1459–70.
- Pietras RJ, Marquez DC, Chen HW, Tsai E, Weinberg O, Fishbein M. Estrogen and growth factor receptor interactions in human breast and non-small cell lung cancer cells. *Steroids* 2005;70:372–81.
- Weinberg OK, Marquez-Garban DC, Fishbein MC, Goodglick L, Garban HJ, Dubinett SM, et al. Aromatase inhibitors in human lung cancer therapy. *Cancer Res* 2005;65:11287–91.
- Mah V, Seligson DB, Li A, Márquez DC, Wistuba II, Elshimali Y, et al. Aromatase expression predicts survival in women with early-stage non-small cell lung cancer. *Cancer Res* 2007;67:10484–90.
- Raso MG, Behrens C, Herynk MH, Liu S, Prudkin L, Ozburn NC, et al. Immunohistochemical expression of estrogen and progesterone receptors identifies a subset of NSCLCs and correlates with *EGFR* mutation. *Clin Cancer Res* 2009;15:5359–68.
- Nose N, Sugio K, Oyama T, Nozoe T, Uramoto H, Iwata T, et al. Association between estrogen receptor- β expression and epidermal growth factor receptor mutation in the postoperative prognosis of adenocarcinoma of the lung. *J Clin Oncol* 2009;27:411–7.
- Stabile LP, Dacic S, Land SR, Lenzner DE, Dhir R, Acquafondata M, et al. Combined analysis of estrogen receptor β -1 and progesterone receptor expression identifies lung cancer patients with poor outcome. *Clin Cancer Res* 2011;17:154–64.
- Liu Y, Inoue M, Sobue T, Tsugane S. Reproductive factors, hormone use and the risk of lung cancer among middle-aged never-smoking Japanese women: a large-scale population-based cohort study. *Int J Cancer* 2005;117:662–6.
- Chlebowski RT, Schwartz AG, Wakelee H, Anderson GL, Stefanick ML, Manson JE, et al. Oestrogen plus progestin and lung cancer in postmenopausal women (Women's Health Initiative trial): a post-hoc analysis of a randomised controlled trial. *Lancet* 2009;374:1243–51.
- Slatore CG, Chien JW, Au DH, Satia JA, White E. Lung cancer and hormone replacement therapy: association in the vitamins and lifestyle study. *J Clin Oncol* 2010;28:1540–6.
- Coombes RC, Hall E, Gibson LJ, Paridaens R, Jassem J, Delozier T, et al. A randomized trial of exemestane after two to three years of tamoxifen therapy in postmenopausal women with primary breast cancer. *N Engl J Med* 2004;350:1081–92.
- Simpson ER, Mahendroo MS, Means GD, Kilgore MW, Hinshelwood MM, Graham-Lorence S, et al. Aromatase cytochrome P450, the enzyme responsible for estrogen biosynthesis. *Endocr Rev* 1994;15:342–55.
- Smith IE, Dowsett M. Aromatase inhibitors in breast cancer. *N Engl J Med* 2003;348:2431–42.
- Niikawa H, Suzuki T, Miki Y, Suzuki S, Nagasaki S, Akahira J, et al. Intratumoral estrogens and estrogen receptors in human non-small cell lung carcinoma. *Clin Cancer Res* 2008;14:4417–26.
- Hershberger PA, Stabile LP, Kanterewicz B, Rothstein ME, Gubish CT, Land S, et al. Estrogen receptor β (ER β) subtype-specific ligands increase transcription, p44/p42 mitogen activated protein kinase (MAPK) activation and growth in human non-small cell lung cancer cells. *J Steroid Biochem Mol Biol* 2009;116:102–9.
- Garon EB, Pietras RJ, Finn RS, Kamranpour N, Pitts S, Márquez-Garban DC, et al. Antiestrogen fulvestrant enhances the anti-proliferative effects of epidermal growth factor receptor inhibitors in human non-small-cell lung cancer. *J Thorac Oncol* 2013;8:270–8.
- Nose N, Uramoto H, Iwata T, Hanagiri T, Yasumoto K. Expression of estrogen receptor β predicts a clinical response and longer progression-free survival after treatment with *EGFR*-TKI for adenocarcinoma of the lung. *Lung Cancer* 2011;71:350–5.
- Sun HB, Zheng Y, Ou W, Fang Q, Li P, Ye X, et al. Association between hormone receptor expression and epidermal growth factor receptor

- mutation in patients operated on for non-small cell lung cancer. *Ann Thorac Surg* 2011;91:1562-7.
28. Travis WD, Brambilla E, Muller-Hermelink HK, Harris CC. Tumours of the lung, pleura, thymus and heart. Pathology and genetics. Lyon: IARC Press; 2004.
 29. Goldstraw P, Crowley J, Chansky K, Giroux DJ, Groome PA, Rami-Porta R, et al. International Association for the Study of Lung Cancer International Staging Committee; Participating Institutions. The IASLC Lung Cancer Staging Project: proposals for the revision of the TNM stage groupings in the forthcoming (seventh) edition of the TNM Classification of Malignant Tumours. *J Thorac Oncol* 2007; 2:706-14.
 30. Nagai Y, Miyazawa H, Huqun, Tanaka T, Udagawa K, Kato M, et al. Genetic heterogeneity of the epidermal growth factor receptor in non-small cell lung cancer cell lines revealed by a rapid and sensitive detection system, the peptide nucleic acid-locked nucleic acid PCR clamp. *Cancer Res* 2005;65:7276-82.
 31. Suda K, Tomizawa K, Fujii M, Murakami H, Osada H, Maehara Y, et al. Epithelial to mesenchymal transition in an epidermal growth factor receptor-mutant lung cancer cell line with acquired resistance to erlotinib. *J Thorac Oncol* 2011;6:1152-61.
 32. Tomizawa K, Suda K, Onozato R, Kuwano H, Yatabe Y, Mitsudomi T. Analysis of ERBB4 mutations and expression in Japanese patients with lung cancer. *J Thorac Oncol* 2010;5:1859-61.
 33. Suda K, Murakami I, Katayama T, Tomizawa K, Osada H, Sekido Y, et al. Reciprocal and complementary role of MET amplification and EGFR T790M mutation in acquired resistance to kinase inhibitors in lung cancer. *Clin Cancer Res* 2010;16:5489-98.
 34. Siegfried JM, Hershberger PA, Stabile LP. Estrogen receptor signaling in lung cancer. *Semin Oncol* 2009;36:524-31.
 35. Verma MK, Miki Y, Sasano H. Aromatase in human lung carcinoma. *Steroids* 2011;76:759-64.
 36. Miki Y, Abe K, Suzuki S, Suzuki T, Sasano H. Suppression of estrogen actions in human lung cancer. *Mol Cell Endocrinol* 2011;340:168-74.
 37. Cheng G, Weihua Z, Warner M, Gustafsson JA. Estrogen receptors ER α and ER β in proliferation in the rodent mammary gland. *Proc Natl Acad Sci U S A* 2004;101:3739-46.
 38. Ishibashi H, Suzuki T, Suzuki S, Niikawa H, Lu L, Miki Y, et al. Progesterone receptor in non-small cell lung cancer—a potent prognostic factor and possible target for endocrine therapy. *Cancer Res* 2005;65:6450-8.
 39. Abe K, Miki Y, Ono K, Mori M, Kakinuma H, Kou Y, et al. Highly concordant coexpression of aromatase and estrogen receptor β in non-small cell lung cancer. *Hum Pathol* 2010;41:190-8.
 40. Oyama T, Kagawa N, Sugio K, Uramoto H, Hatano O, Harada N, et al. Expression of aromatase CYP19 and its relationship with parameters in NSCLC. *Front Biosci* 2009;14:2285-92.
 41. Koutras A, Giannopoulou E, Kritikou I, Antonacopoulou A, Evans TR, Papavasiliou AG, et al. Antiproliferative effect of exemestane in lung cancer cells. *Mol Cancer* 2009;24:109.
 42. Marquez-Garban DC, Chen HW, Fishbein MC, Goodglick L, Pietras RJ. Estrogen receptor signaling pathways in human non-small cell lung cancer. *Steroids* 2007;72:135-43.
 43. Márquez-Garbán DC, Chen HW, Goodglick L, Fishbein MC, Pietras RJ. Targeting aromatase and estrogen signaling in human non-small cell lung cancer. *Ann NY Acad Sci* 2009;1155:194-205.
 44. Miki Y, Suzuki T, Abe K, Suzuki S, Niikawa H, Iida S, et al. Intratumoral localization of aromatase and interaction between stromal and parenchymal cells in the non-small cell lung carcinoma microenvironment. *Cancer Res* 2010;70:6659-69.
 45. Traynor AM, Schiller JH, Stabile LP, Kolesar JM, Eickhoff JC, Dacic S, et al. Pilot study of gefitinib and fulvestrant in the treatment of postmenopausal women with advanced non-small cell lung cancer. *Lung Cancer* 2009;64:51-9.

Clinical Cancer Research

Prognostic and Therapeutic Implications of Aromatase Expression in Lung Adenocarcinomas with *EGFR* Mutations

Mikihiro Kohno, Tatsuro Okamoto, Kenichi Suda, et al.

Clin Cancer Res 2014;20:3613-3622. Published OnlineFirst May 6, 2014.

Updated version Access the most recent version of this article at:
[doi:10.1158/1078-0432.CCR-13-2683](https://doi.org/10.1158/1078-0432.CCR-13-2683)

Supplementary Material Access the most recent supplemental material at:
<http://clincancerres.aacrjournals.org/content/suppl/2014/05/07/1078-0432.CCR-13-2683.DC1.html>

Cited Articles This article cites by 44 articles, 18 of which you can access for free at:
<http://clincancerres.aacrjournals.org/content/20/13/3613.full.html#ref-list-1>

Citing articles This article has been cited by 1 HighWire-hosted articles. Access the articles at:
<http://clincancerres.aacrjournals.org/content/20/13/3613.full.html#related-urls>

E-mail alerts Sign up to receive free email-alerts related to this article or journal.

Reprints and Subscriptions To order reprints of this article or to subscribe to the journal, contact the AACR Publications Department at pubs@aacr.org.

Permissions To request permission to re-use all or part of this article, contact the AACR Publications Department at permissions@aacr.org.

Ultra-low-dose CT of the Lung:

Effect of Iterative Reconstruction Techniques on Image Quality

Masahiro Yanagawa, MD, PhD, Tomoko Gyobu, MD, Ann N. Leung, MD, Misa Kawai, MD, Yutaka Kawata, MD, Hiromitsu Sumikawa, MD, PhD, Osamu Honda, MD, PhD, Noriyuki Tomiyama, MD, PhD

Rationale and Objectives: To compare quality of ultra-low-dose thin-section computed tomography (CT) images of the lung reconstructed using model-based iterative reconstruction (MBIR) and adaptive statistical iterative reconstruction (ASIR) to filtered back projection (FBP) and to determine the minimum tube current–time product on MBIR images by comparing to standard-dose FBP images.

Materials and Methods: Ten cadaveric lungs were scanned using 120 kVp and four different tube current–time products (8, 16, 32, and 80 mAs). Thin-section images were reconstructed using MBIR, three ASIR blends (30%, 60%, and 90%), and FBP. Using the 8-mAs data, side-to-side comparison of the four iterative reconstruction image sets to FBP was performed by two independent observers who evaluated normal and abnormal findings, subjective image noise, streak artifact, and overall image quality. Image noise was also measured quantitatively. Subsequently, 8-, 16-, and 32-mAs MBIR images were compared to standard-dose FBP images. Comparisons of image sets were analyzed using the Wilcoxon signed rank test with Bonferroni correction.

Results: At 8 mAs, MBIR images were significantly better ($P < .005$) than other reconstruction techniques except in evaluation of interlobular septal thickening. Each set of low-dose MBIR images had significantly lower ($P < .001$) subjective and objective noise and streak artifacts than standard-dose FBP images. Conspicuity and visibility of normal and abnormal findings were not significantly different between 16-mAs MBIR and 80-mAs FBP images except in identification of intralobular reticular opacities.

Conclusions: MBIR imaging shows higher overall quality with lower noise and streak artifacts than ASIR or FBP imaging, resulting in nearly 80% dose reduction without any degradations of overall image quality.

Key Words: Radiation dose reduction; model-based iterative reconstruction; adaptive statistical iterative reconstruction; filtered back projection; image quality.

©AUR, 2014

The increase of the radiation dose delivered in computed tomography (CT) has recently been a problem. Because there is a trade-off between image quality and radiation dose on CT, however, it is not always appropriate to decrease radiation dose on CT. Iterative reconstruction algorithms for CT have been developed by multiple equipment manufacturers to reduce image noise associated with radiation dose reduction (1–8). Adaptive statistical iterative reconstruction (ASIR) and model-based iterative reconstruction (MBIR) are types of iterative reconstruction algorithms available on clinical settings. The ASIR technique models photon and electronic noise statistics; by partially correcting for fluctuations in projection measurements due to limited photon statistics, ASIR enables a time-efficient reduc-

tion in pixel variance that is statistically unlikely to be representative of anatomic features resulting in a reduction of image noise with no decrement in spatial resolution (9). In clinical practice, ASIR is typically used in combination with the standard filtered back projection (FBP) reconstruction to create blended images. As compared to ASIR, MBIR is a more mathematically complex and time-consuming technique as it models not only system statistics but also system optics (10). Phantom experiments show that MBIR has potential to improve spatial resolution and allow further reductions in image noise (9). To date, few studies have evaluated CT image quality of the lung using MBIR (10–14). Thus, unlike FBP and ASIR, MBIR technique might have the potential not to degrade image quality even under the extreme dose reduction. McCollough et al. (15) reported that the advances in data acquisition, image reconstruction, and optimization processes that were identified by consensus as being necessary to achieve submillisievert-dose CT examinations. It is expected that MBIR might be one of techniques to enable a submillisievert-dose CT. The present study was performed using cadaveric lung models that can provide multiple acquisitions to determine the minimum tube current–time product at which image quality of a low-dose MBIR study is comparable to that of a standard-dose FBP study. The aim of this present study was two-fold: to compare quality of ultra-low-dose

Acad Radiol 2014; 21:695–703

From the Department of Diagnostic Radiology, Stanford University School of Medicine, 1201 Welch Rd, Stanford, CA 94305 (M.Y., A.N.L.); Department of Radiology, Osaka University Graduate School of Medicine, Suita, Osaka, Japan (M.Y., T.G., M.K., H.S., O.H., N.T.); and Department of Radiology, Osaka Rosai Hospital, Sakai, Osaka, Japan (Y.K.). Received December 2, 2013; accepted January 31, 2014. All authors declare that there is no conflict of interest. **Address correspondence to:** M.Y. e-mail: masayana@stanford.edu or m-yanagawa@radiol.med.osaka-u.ac.jp

©AUR, 2014

<http://dx.doi.org/10.1016/j.acra.2014.01.023>

thin-section CT images of the lung reconstructed using MBIR and ASIR to FBP and to determine the minimum tube current-time product at which image quality of an MBIR study is comparable to that of a standard-dose FBP.

MATERIALS AND METHODS

Cadaveric Lungs and Imaging

We obtained approval from our internal Ethics Review Board. Informed consent was obtained for the use of patient biomaterial and for retrospective review of patient records and images. Ten cadaveric lungs were inflated and fixed by the method of Heitzman (16). These lungs were distended through the main bronchus with fixative fluid that contained polyethylene glycol 400, 95% ethyl alcohol, 40% formalin, and water in the proportions of 10:5:2:3. The specimens were immersed in fixative for 2 days and the lungs were then air dried. The pathologic diagnoses of these 10 lungs were usual interstitial pneumonia ($n = 1$), diffuse alveolar damage ($n = 1$), diffuse panbronchiolitis ($n = 1$), pneumonia ($n = 2$), emphysema ($n = 1$), diffuse alveolar hemorrhage ($n = 1$), metastatic disease ($n = 2$), and lymphangitic carcinomatosis ($n = 1$).

The 10 lungs were scanned on a multi-detector row CT (MDCT) scanner (Discovery CT750HD; GE Healthcare Technologies, Milwaukee, WI). CT protocol was as follows: detector collimation, 0.625 mm; detector pitch, 0.984; gantry rotation period, 0.4 seconds; matrix size, 512×512 pixels; 30-cm scan length; x-ray voltage, 120 kVp; tube current, 20, 40, 80, and 200 mA; and non-high-resolution mode with 984 views per rotation. Both ASIR and MBIR are part of the commercially available package implemented on the control panel of the CT scanner.

Axial thin-section CT images of 0.625 mm thickness and 20 cm field of view were reconstructed with MBIR, ASIR (30%, 60%, and 90% [represented as ASIR₃₀, ASIR₆₀, and ASIR₉₀]), and FBP. The voxel dimensions of CT image are $0.391 \times 0.391 \times 0.625$ mm. A high-spatial-frequency algorithm was used in ASIR and FBP; however, there was no concept of reconstruction algorithm in MBIR. Based on lung cancer screening literature (17) that defines a tube current-time product of 40 mAs as "low dose", we use the term "ultra-low-dose" CT to refer to studies acquired with tube current-time products ≤ 20 mAs and result in an effective dose of < 1 mSv.

Subjective Image Analysis

Three to four cross-sectional levels with the most conspicuous CT findings were chosen from each cadaveric lung by the principal investigator (M.Y., with 12 years of experience): three images were selected for seven lungs and four images for the remaining three lungs. There were a total of 264 images, that is, 33 sets of 8 image series (8-mAs, 16-mAs, and 32-mAs MBIR, 8-mAs ASIR₃₀, 8-mAs ASIR₆₀, 8-mAs ASIR₉₀, and 8-mAs and 80-mAs FBP).

TABLE 1. Radiation Dose Descriptions

	Low Dose			Standard Dose
	8 mAs	16 mAs	32 mAs	80 mAs
CTDIvol (mGy)	0.65	1.30	2.59	6.49
DLP (mGy-cm)	22.15	44.30	88.60	221.50
ED (mSv)	0.31	0.62	1.24	3.10

CTDIvol, computed tomography dose index volume; DLP, dose-length product; ED, effective dose.

Two independent chest radiologists (M.K. and Y.K., with 8 years of experience each) without prior knowledge of the pathologic diagnoses, image acquisition parameters, or iterative reconstruction techniques reviewed the 264 images on a 5-megapixel 21-in monochrome liquid-crystal display monitor. All images were displayed at a window level of -700 Hounsfield units (HU) and a window width of 1200 HU. In the first step, 8-mAs MBIR and 8-mAs ASIR were compared to 8-mAs FBP. Approximately 1 month later, in the second step, 8-mAs, 16-mAs, and 32-mAs MBIR were compared to 80-mAs FBP.

The two observers compared the conspicuity and visibility of normal (central and peripheral vessels, central and peripheral airways, and interlobar fissures) and abnormal (ground-glass opacity [GGO], consolidation, nodules, interlobular septal thickening, intralobular reticulation, cyst, and bronchiectasis) CT findings using a five-point scale as compared to the FBP image: (1) an unacceptable image on which it was more difficult to detect and/or visualize findings in whole lung; (2) an inferior image on which it was more difficult to detect and/or visualize findings in at least one area of the lung; (3) an image comparable to the FBP image; (4) a superior image on which it was easier to detect and/or visualize findings in at least one area of the lung; and (5) an excellent image on which it was easier to detect and/or visualize findings in whole lung. Subjective visual noise and streak artifact were also graded on a five-point comparative scale: (1) noise/artifact significantly worse, nondiagnostic; (2) noise/artifact worse; (3) similar noise/artifact compared to image of FBP; (4) noise/artifact improved; and (5) noise/artifact significantly improved, almost nondetectable. Overall image quality was finally graded on a five-point scale: (1) unacceptable, nondiagnostic; (2) inferior; (3) comparable to the FBP image; (4) better; and (5) excellent. If there were different scores between two observers, final evaluation was decided by an adjudicator (H.S., with 13 years of experience).

Objective Image Analysis

Quantitative noise measurements were calculated by measuring the standard deviation (SD) in a circular region of interest (ROI) defined by an electric cursor, using free software (ImageJ version 1.37v; NIH, Bethesda, MD; for further information regarding ImageJ software, see <http://rsb.info.nih.gov/ij/index.html>). Quantitative noise measurements

TABLE 2. Comparison among FBP, ASIR, and MBIR on Ultra-low-dose (8 mAs) CT

	Normal Findings			Abnormal Findings			Other Findings		Overall Image Quality
	Central Vessels and Airways	Peripheral Vessels and Airways	Interlobar Fissures	Nodules	GGO	ISP	Image Noise	Streak Artifact	
Reconstruction technique									
MBIR	4.83 ± 0.07	4.68 ± 0.09	4.75 ± 0.11	4.96 ± 0.04	4.84 ± 0.07	4.19 ± 0.16	5.00 ± 0.00	5.00 ± 0.00	4.97 ± 0.03
ASIR ₉₀	4.06 ± 0.11	4.04 ± 0.07	4.00 ± 0.13	4.00 ± 0.05	4.16 ± 0.07	3.88 ± 0.09	4.21 ± 0.07	4.03 ± 0.12	4.55 ± 0.09
ASIR ₆₀	3.52 ± 0.09	3.32 ± 0.09	3.19 ± 0.10	3.39 ± 0.09	3.84 ± 0.07	3.31 ± 0.12	3.73 ± 0.08	3.45 ± 0.09	3.55 ± 0.09
ASIR ₃₀	3.00 ± 0.00	3.00 ± 0.00	3.00 ± 0.00	3.04 ± 0.04	3.04 ± 0.04	3.00 ± 0.00	3.03 ± 0.03	3.00 ± 0.00	3.00 ± 0.00
FBP	3.00 ± 0.00	3.00 ± 0.00	3.00 ± 0.00	3.00 ± 0.00	3.00 ± 0.00	3.00 ± 0.00	3.00 ± 0.00	3.00 ± 0.00	3.00 ± 0.00
Pairwise comparison (<i>P</i> [*])									
MBIR versus ASIR ₉₀	<.001	<.001	.005	<.001	<.001	.962	<.001	<.001	<.001
ASIR ₆₀	<.001	<.001	<.001	<.001	<.001	.002	<.001	<.001	<.001
ASIR ₃₀	<.001	<.001	<.001	<.001	<.001	<.001	<.001	<.001	<.001
FBP	<.001	<.001	<.001	<.001	<.001	<.001	<.001	<.001	<.001
ASIR ₉₀ versus ASIR ₆₀	<.001	<.001	<.001	<.001	.084	.005	<.001	<.001	<.001
ASIR ₃₀	<.001	<.001	<.001	<.001	<.001	<.001	<.001	<.001	<.001
FBP	<.001	<.001	<.001	<.001	<.001	<.001	<.001	<.001	<.001
ASIR ₆₀ versus ASIR ₃₀	<.001	.026	.825	.006	<.001	.197	<.001	<.001	<.001
FBP	<.001	.026	.825	.003	<.001	.197	<.001	<.001	<.001
ASIR ₃₀ versus FBP	1.000	1.000	1.000	1.000	1.000	1.000	1.000	1.000	1.000

ASIR, adaptive statistical iterative reconstruction; GGO, ground-glass opacity; ISP, interlobular septal thickening; FBP, filtered back projection; MBIR, model-based iterative reconstruction. Data are presented as mean ± standard deviation. Data of the subjective image analysis were statistically analyzed using the Wilcoxon signed rank tests with a Bonferroni correction applied for multiple comparisons. *P*^{*} is a Bonferroni-corrected *P* value. *P*^{*} value <.05 was considered to be significant.

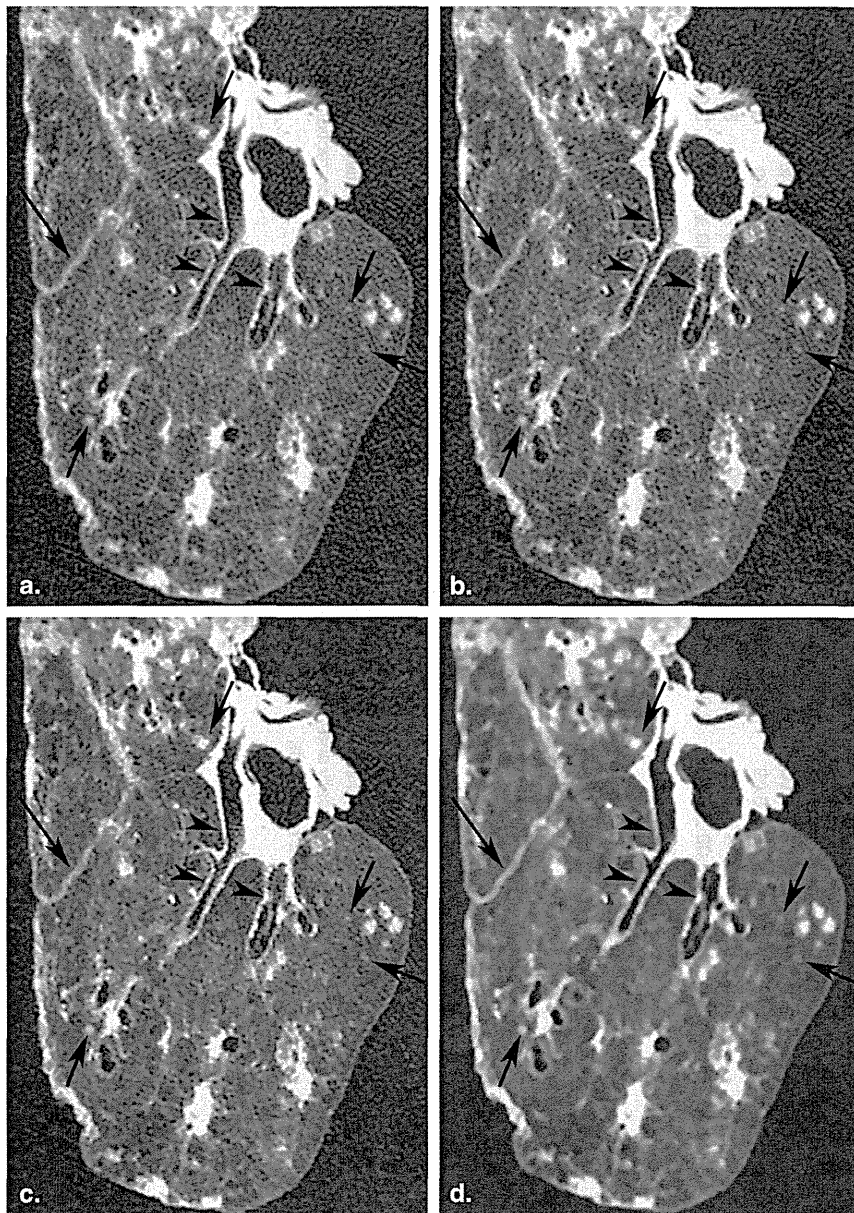


Figure 1. Ultra-low-dose (8 mAs) thin-section computed tomographic images of a cadaveric lung with diffuse panbronchiolitis show serial improvement in image noise and streak artifacts in following ascending order: FBP (a), ASIR₃₀ (b), ASIR₉₀ (c), and MBIR (d). With almost no perceptible noise or streak artifact on MBIR image, conspicuity and visibility of the fissure (*long arrow*), small nodules (*short arrows*), and bronchial walls (*arrowheads*) are improved as compared to FBP or ASIR blends. Note the blotchy pixilated appearance of the MBIR images. ASIR, adaptive statistical iterative reconstruction; FBP, filtered back projection; MBIR, model-based iterative reconstruction.

were obtained in the air adjacent to the lung specimen (18,19). An ROI (200 mm²) was placed in four homogeneous parts of an image and was confirmed to be in exactly the same location on each image of a series by a collaborator (T.G., with 8 years of experience). Average values of SD were analyzed statistically.

Statistical Analysis

All statistical analyses were performed using commercially available software (MedCalc version 12.3.0.0 statistical software; Frank Schoonjans, Mariakerke, Belgium). Agreement between two observers in each evaluated category of CT findings was evaluated using the κ statistic and classified as poor ($\kappa = 0.00-0.20$), fair ($\kappa = 0.21-0.40$), moderate ($\kappa = 0.41-0.60$), good ($\kappa = 0.61-0.80$), or excellent ($\kappa = 0.81-1.00$).

Data of the subjective image analysis were statistically analyzed using the Wilcoxon signed rank tests, which was conducted with Bonferroni correction applied for multiple comparisons. On the other hand, data of the objective image analysis were statistically analyzed using repeated measures analysis of variance pairwise comparison methods (Student's paired *t* test) with Bonferroni correction. A Bonferroni-corrected *P* value of <0.05 was considered significant.

RESULTS

Radiation Doses

Radiation dose measurements associated with low-dose (8, 16, and 32 mAs) and standard-dose (80 mAs) techniques

TABLE 3. Comparison between 8-mAs, 16-mAs, and 32-mAs MBIR Versus 80-mAs FBP

	Normal Findings			Abnormal Findings			Other Findings		Overall Image Quality
	Central Vessels and Airways	Peripheral Vessels and Airways	Interlobar Fissures	Nodules	GGO	ISP	Image Noise	Streak Artifact	
Reconstruction technique									
32-mAs MBIR	3.33 ± 0.09	3.50 ± 0.11	3.53 ± 0.17	3.46 ± 0.09	3.77 ± 0.11	3.44 ± 0.13	4.97 ± 0.03	4.97 ± 0.03	3.67 ± 0.12
16-mAs-MBIR	3.07 ± 0.07	3.14 ± 0.14	3.27 ± 0.12	3.18 ± 0.10	3.27 ± 0.13	2.75 ± 0.17	4.93 ± 0.05	4.93 ± 0.05	2.93 ± 0.08
8-mAs MBIR	3.07 ± 0.07	2.73 ± 0.18	2.93 ± 0.07	2.82 ± 0.12	2.86 ± 0.12	2.19 ± 0.10	4.87 ± 0.06	4.93 ± 0.05	2.63 ± 0.10
80-mAs FBP	3.00 ± 0.00	3.00 ± 0.00	3.00 ± 0.00	3.00 ± 0.00	3.00 ± 0.00	3.00 ± 0.00	3.00 ± 0.00	3.00 ± 0.00	3.00 ± 0.00
Pairwise comparison (<i>P</i> [*])									
32-mAs MBIR versus 16-mAs MBIR	.179	.047	.243	.108	.005	.002	1.000	1.000	<.001
8-mAs MBIR	.179	<.001	.015	.001	<.001	<.001	1.000	1.000	<.001
80-mAs FBP	.004	.001	.037	<.001	<.001	.023	<.001	<.001	<.001
16-mAs MBIR versus 8-mAs MBIR	1.000	.023	.115	.013	.023	.017	.965	1.000	.028
80-mAs FBP	1.000	1.000	.243	.576	.333	.983	<.001	<.001	1.000
8-mAs MBIR versus 80-mAs FBP	1.000	.821	1.000	.805	1.000	<.001	<.001	<.001	.007

ASIR, adaptive statistical iterative reconstruction; GGO, ground-glass opacity; ISP, interlobular septal thickening; FBP, filtered back projection; MBIR, model-based iterative reconstruction. Data are presented as mean ± standard deviation. Data of the subjective image analysis were statistically analyzed using the Wilcoxon signed rank tests with a Bonferroni correction applied for multiple comparisons. *P*^{*} is a Bonferroni-corrected *P* value. *P*^{*} value <0.05 was considered to be significant.

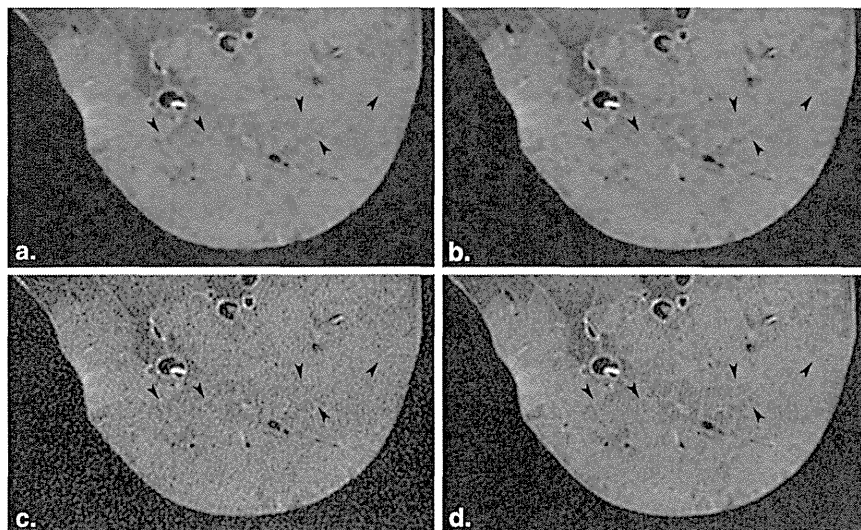


Figure 2. Thin-section computed tomographic images of a cadaveric lung with diffuse alveolar hemorrhage show diminished visibility of intralobular reticular opacities (arrowheads) on (a) 8-mAs and (b) 16-mAs MBIR images as compared to (c) 8-mAs and (d) 80-mAs FBP despite their higher noise levels. FBP, filtered back projection; MBIR, model-based iterative reconstruction.

used in scanning of the 10 cadaveric lungs are summarized in Table 1. The reported radiation dose measurements consist of CT dose index volume (CTDI_{vol}), dose-length product (DLP), and effective dose (ED) which was calculated as the product of DLP and 'k' conversion coefficient (0.014 mSv/[mGy cm]) for chest CT (20). Compared to standard-dose (80 mAs) technique, there were 80% and 90% decreases in dose measurements for 16-mAs and 8-mAs acquisitions, respectively with effective doses in the submillisievert range (0.31 and 0.62).

Subjective Evaluation of CT Findings

Comparisons between images reconstructed using MBIR, ASIR blends, and FBP and acquired at 8 mAs are summarized in Table 2. Statistical analysis of four findings (consolidation, intralobular reticular opacities, cyst, and bronchiectasis) could not be performed because of their low prevalence (<2% of cases). Interobserver agreement for each evaluated category of CT findings was from moderate to excellent ($\kappa = 0.46$ –1.00). There were no kappa values in the following eight items because all the same scores were graded by two observers: on MBIR images, other findings (image noise and streak artifact); on ASIR₃₀ images, normal findings (central vessels and airways, peripheral vessels and airways, and interlobar fissures), interlobular septal thickening, streak artifacts, and overall image quality. In each evaluated category of CT findings, MBIR scored highest with significant differences between MBIR, ASIR blends, and FBP except for interlobular septal thickening, which was not significantly different between MBIR and ASIR₉₀. ASIR₉₀ images scored significantly higher in each category than the two lower ASIR blends or FBP except for GGO, which was not statistically different from ASIR₆₀ ($P = .084$). Conspicuity and visibility of CT findings using ASIR₃₀ were equivalent to FBP ($P = 1.000$; Fig. 1). Scores

for subjective image noise and streak artifact significantly improved with increasing blends of ASIR ($P < .001$).

Comparisons between low-dose MBIR and standard-dose FBP images are summarized in Table 3. Interobserver agreement for each evaluated category of CT findings was from moderate to excellent ($\kappa = 0.42$ –0.83). In each evaluated category of CT findings, 32-mAs MBIR scored highest with significant improvements in finding conspicuity, image noise, streak artifact, and overall image quality as compared to FBP ($P \leq .037$). Comparisons between ultra-low-dose (8 and 16 mAs) MBIR and 80-mAs FBP showed no statistically significant difference in conspicuity or visibility of normal and abnormal CT findings with the exception of interlobular septal thickening which was less well visualized on 8-mAs MBIR than on FBP ($P < .001$). A decrease in conspicuity of intralobular reticular opacities was identified by both observers on ultra-low-dose MBIR (Fig. 2) although formal statistical analysis could not be performed because of low prevalence of this finding. Scores for subjective image noise and streak artifact significantly improved on 8-mAs and 16-mAs MBIR images as compared to standard-dose FBP ($P < .001$), but with no significant differences among the three different dose MBIR image sets. Overall image quality was equivalent for 16-mAs MBIR ($P = 1.00$; Fig. 3) but inferior for 8-mAs MBIR ($P = .028$) as compared to FBP.

Quantitative Image Noise Measurements

Figure 4 shows sequential and statistically significant decreases ($P < .001$) in objective image noise on 8-mAs images reconstructed with FBP, increasing blends of ASIR, and MBIR. Figure 5 similarly shows sequential and statistically significant decreases ($P < .001$) in objective image noise on images acquired and reconstructed using 80-mAs FBP and 8-, 16-, and 32-mAs MBIR.

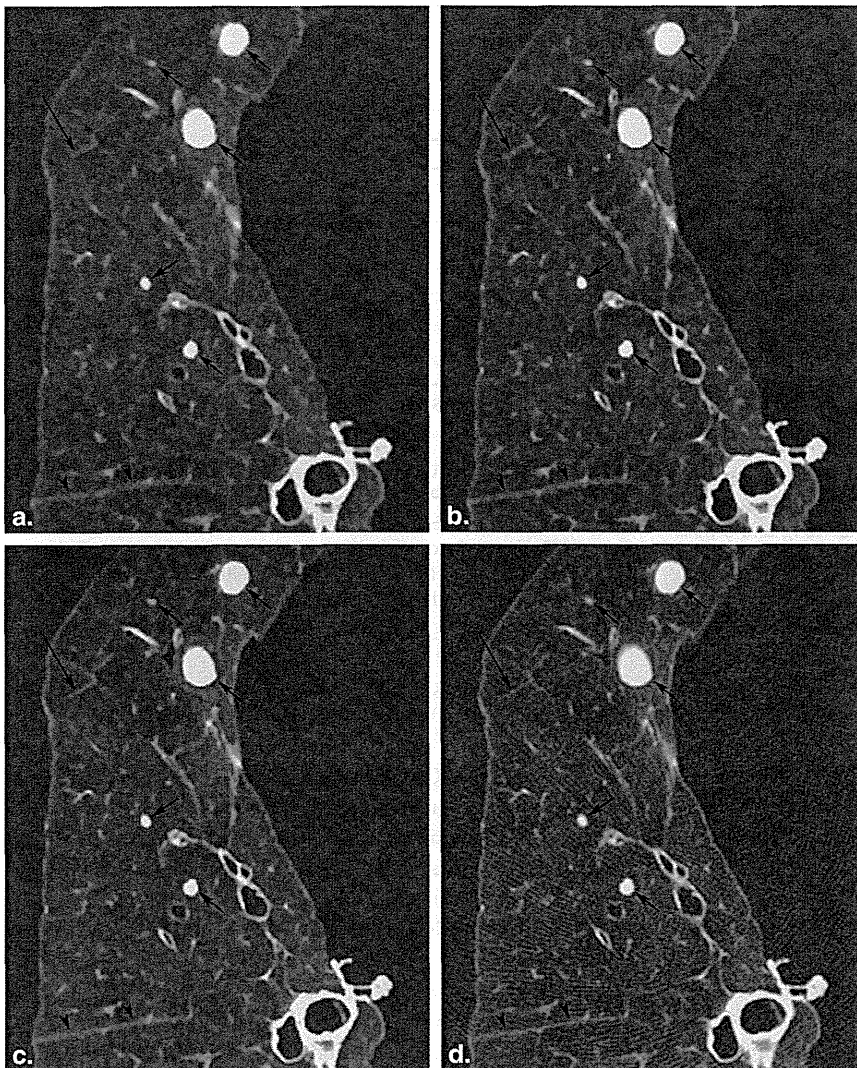


Figure 3. Thin-section computed tomographic images of a cadaveric lung with metastases acquired and reconstructed using 8-mAs MBIR (a), 16-mAs MBIR (b), 32-mAs MBIR (c), and 80-mAs FBP (d) show similar low level of noise and streak artifacts on the three MBIR images, irrespective of dose. Conspicuity and visibility of peripheral vessels (*long arrow*), interlobar fissure (*arrowheads*), and margins of small and large nodules (*short arrows*) are worse on 8-mAs (a), similar on 16-mAs (b), and better on 32-mAs MBIR (c) images as compared to standard-dose FBP (d). FBP, filtered back projection; MBIR, model-based iterative reconstruction.

DISCUSSION

The principle of ALARA (as low as reasonably achievable) urges radiologists to use the minimum level of radiation needed in imaging examinations to achieve the necessary diagnostic results. Iterative reconstruction algorithms are one of the newer options in the available dose reduction armamentarium that has included restriction of length of coverage, reduced tube voltage, and tube current modulation (11). Of the two iterative reconstruction algorithms evaluated in this study, ASIR, which was introduced earlier, has been more extensively studied (1–8,21–23) and has now largely been implemented into routine clinical practice. In comparison, MBIR, a more mathematically complex reconstruction technique, offers greater potential in dose reduction but at the cost of longer reconstruction times on the order of 45–60 minutes per series (10,11,24). Few studies to date (10–14) have evaluated image quality and diagnostic adequacy of ultra-low-dose MBIR for thin-section chest CT studies.

Our study showed that both ASIR and MBIR can improve lung image quality on ultra-low-dose CT as compared to FBP with MBIR images rated highest. These results are consistent with those of prior clinical studies (10,14) that have reported that when scanning at submillisievert doses, MBIR is superior to ASIR in generating diagnostically acceptable thin-section chest CT images largely because of marked reductions in image noise.

Of the four different iterative reconstructions performed in our study, overall image quality, image noise, and streak artifact were each rated best for MBIR and sequentially decreased with lower blends of ASIR ($ASIR_{90} > ASIR_{60} > ASIR_{30}$). Although a pixilated blotchy appearance has previously been described in association with high-percentage ASIR blends (6,22), this feature was not observed in this study likely related to interval improvements of the ASIR algorithm by the vendor (10). A blotchy appearance however was characteristic of MBIR images, which rendered blinding of

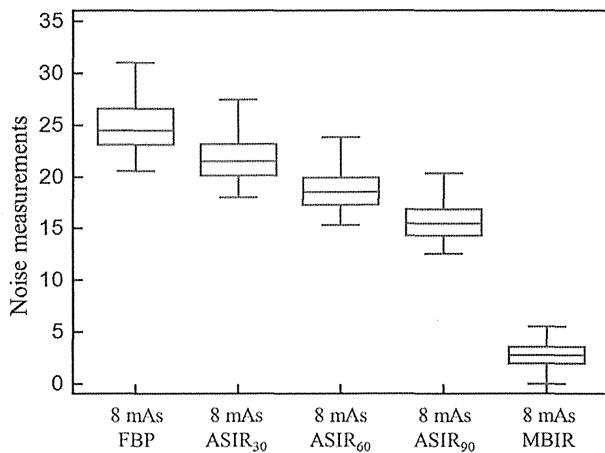


Figure 4. Quantitative noise measurements (mean \pm standard deviation): 8-mAs FBP (24.7 ± 2.21), 8-mAs ASIR₃₀ (21.6 ± 2.01), 8-mAs ASIR₆₀ (18.5 ± 1.81), 8-mAs ASIR₉₀ (15.5 ± 1.64), and 8-mAs MBIR (2.71 ± 1.10). Significant differences in quantitative noise measurements were found among all groups ($P < .001$). ASIR, adaptive statistical iterative reconstruction; FBP, filtered back projection; MBIR, model-based iterative reconstruction.

observers impossible but did not adversely impact conspicuity or visibility of the CT findings evaluated in this study, namely central and peripheral airways and vessels, interlobar fissures, nodules, GGOs, and thickened interlobular septa. We did, however, observe obscuration of intralobular reticular opacities on MBIR images of one lung specimen with a “crazing paving” pattern because of diffuse alveolar hemorrhage. We postulate that visibility of these fine low-contrast abnormalities may be decreased on the ultra-low-dose MBIR images. Further research on diagnostic adequacy of low-dose MBIR images for broader spectrum of lung abnormalities including those of intrinsic low contrast is required before this technique can be adopted into routine clinical practice.

Although not possible in clinical patients, using this cadaveric lung model, we were able to perform multiple acquisitions to determine the minimum tube current–time product at which image quality of a low-dose MBIR study is comparable to that of a standard-dose FBP study. Of the three tube currents tested, 32-mAs MBIR images were rated highest with statistically significant improvements in conspicuity of each evaluated category of normal and abnormal CT findings, level of image noise, presence of streak artifact, and overall image quality. We found no significant difference in conspicuity of evaluated CT findings (GGOs, nodules, and interlobular septa) between 16-mAs MBIR as compared to 80-mAs FBP despite an 80% reduction in effective dose. At 90% dose reduction, significant decreases in overall image quality and conspicuity of interlobular septal thickening were observed on 8-mAs MBIR images. Thus, MBIR technique enables a submillisievert-dose (0.62 mSv) CT. This effective dose, which is well below the annual exposure from natural sources (3.1 mSv/year), is only 10 times greater than that delivered with two-view radiography (0.06 mSv for standard

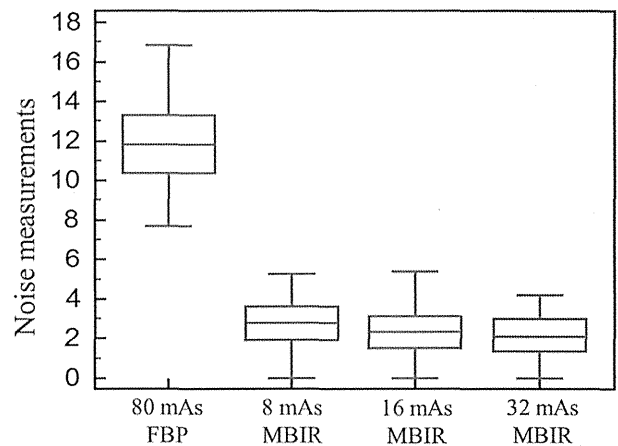


Figure 5. Quantitative noise measurements (mean \pm standard deviation): 80-mAs FBP (11.99 ± 2.01), 8-mAs MBIR (2.73 ± 1.11), 16-mAs MBIR (2.42 ± 1.10), and 32-mAs MBIR (2.12 ± 1.10). Significant differences in quantitative noise measurements were found among all groups ($P < .001$). FBP, filtered back projection; MBIR = model-based iterative reconstruction.

patient), including posteroanterior- and lateral-projection acquisitions (15,25).

Neroladaki et al. (14) have similarly reported limitations in detection of some CT findings on ultra-low-dose MBIR images that were acquired in their study at a radiation exposure (100 kVp, 6 mAs) similar to chest radiography. High-contrast lesions such as solid nodules and architectural distortion were consistently identified by three observers, while interobserver agreement for GGOs and emphysema were fair and poor, respectively.

Detectability of nodules on ultra-low-dose MBIR has been investigated by several groups (11,12,14). Using low-dose (50 mAs) FBP as the gold standard, Yamada et al. (12) report average true-positive fractions of 1.0 and 0.944 for calcified and ≥ 4 mm noncalcified nodules, respectively on ultra-low-dose (4 mAs) MBIR. Katsura et al. (11) compared 5-mAs MBIR to low-dose ASIR₅₀ and found no significant differences in detection of nodules ≥ 4 mm including nodules with nonsolid components; however, as compared to reference dose ASIR₅₀, only an average of 10.5 of 18 pure ground-glass nodules were identified on ultra-low-dose MBIR by the two observers.

Our study was limited by the small number of cases with only three types of abnormal CT findings included for formal evaluation; determination of the diagnostic adequacy of ultra-low-dose MBIR technique will require larger sample sizes with inclusion of a broader spectrum of representative lung CT findings that are encountered in clinical practice. The use of a cadaveric lung model did not allow us to evaluate the influence of a chest wall, body habitus, or motion artifacts on image quality. Moreover, histologic sections of cadaveric lungs should have been used to evaluate the fidelity of the various CT images. Because ASIR and MBIR algorithms are both manufactured by the same company, it is unclear as

to whether the results of our studies are applicable to other iterative reconstruction algorithms. Finally, although the image data sets used in the present study were randomized, perfect blinding to MBIR images might be difficult because it may be relatively easy to discriminate MBIR images with no concept of reconstruction algorithm from ASIR and FBP using a high-spatial-frequency algorithm.

In conclusion, ultra-low-dose thin-section CT images of the lung reconstructed using MBIR are of higher overall image quality with less noise and streak artifact than images reconstructed using ASIR. Even nearly 80% dose reduction under the use of MBIR does not degrade overall image quality.

REFERENCES

- Prakash P, Kalra MK, Kambadakone AK, et al. Reducing abdominal CT radiation dose with adaptive statistical iterative reconstruction technique. *Invest Radiol* 2010; 45:202–210.
- Singh S, Kalra MK, Hsieh J, et al. Abdominal CT: comparison of adaptive statistical iterative and filtered back projection reconstruction techniques. *Radiology* 2010; 257:373–383.
- Honda O, Yanagawa M, Inoue A, et al. Image quality of multiplanar reconstruction of pulmonary CT scans using adaptive statistical iterative reconstruction. *Br J Radiol* 2011; 84:335–341.
- Gervaise A, Osemont B, Lecocq S, et al. CT image quality improvement using Adaptive Iterative Dose Reduction with wide-volume acquisition on 320-detector CT. *Eur Radiol* 2012; 22:295–301.
- Prakash P, Kalra MK, Ackman JB, et al. Diffuse lung disease: CT of the chest with adaptive statistical iterative reconstruction technique. *Radiology* 2010; 256:261–269.
- Singh S, Kalra MK, Gilman MD, et al. Adaptive statistical iterative reconstruction technique for radiation dose reduction in chest CT: a pilot study. *Radiology* 2011; 259:565–573.
- Funama Y, Taguchi K, Utsunomiya D, et al. Combination of a low-tube-voltage technique with hybrid iterative reconstruction (iDose) algorithm at coronary computed tomographic angiography. *J Comput Assist Tomogr* 2011; 35:480–485.
- Moscariello A, Takx RA, Schoepf UJ, et al. Coronary CT angiography: image quality, diagnostic accuracy, and potential for radiation dose reduction using a novel iterative image reconstruction technique—comparison with traditional filtered back projection. *Eur Radiol* 2011; 21:2130–2138.
- Thibault JB, Sauer KD, Bouman CA, et al. A three-dimensional statistical approach to improved image quality for multislice helical CT. *Med Phys* 2007; 34:4526–4544.
- Katsura M, Matsuda I, Akahane M, et al. Model-based iterative reconstruction technique for radiation dose reduction in chest CT: comparison with the adaptive statistical iterative reconstruction technique. *Eur Radiol* 2012; 22:1613–1623.
- Katsura M, Matsuda I, Akahane M, et al. Model-based iterative reconstruction technique for ultralow-dose chest CT: comparison of pulmonary nodule detectability with the adaptive statistical iterative reconstruction technique. *Invest Radiol* 2013; 48:206–212.
- Yamada Y, Jinzaki M, Tanami Y, et al. Model-based iterative reconstruction technique for ultralow-dose computed tomography of the lung: a pilot study. *Invest Radiol* 2012; 47:482–489.
- Vardhanabhuti V, Loader RJ, Mitchell GR, et al. Image quality assessment of standard- and low-dose chest CT using filtered back projection, adaptive statistical iterative reconstruction, and novel model-based iterative reconstruction algorithms. *AJR Am J Roentgenol* 2013; 200:545–552.
- Neroladaki A, Botsikas D, Boudabbous S, et al. Computed tomography of the chest with model-based iterative reconstruction using a radiation exposure similar to chest X-ray examination: preliminary observations. *Eur Radiol* 2013; 23:360–366.
- McCollough CH, Chen GH, Kalender W, et al. Achieving routine submillisievert CT scanning: report from the summit on management of radiation dose in CT. *Radiology* 2012; 264:567–580.
- Markarian B, Dailey ET. Preparation of inflated lung specimens. In: Groskin SA, ed. *Heitzman's The lung: radiologic-pathologic correlations*. 3rd ed. St. Louis: Mosby, 1993; 4–12.
- Aberle DR, Berg CD, Black WC, et al. The National Lung Screening Trial: overview and study design. *Radiology* 2011; 258:243–253.
- Boehm T, Willmann JK, Hilfiker PR, et al. Thin-section CT of the lung: dose electrocardiographic triggering influence diagnosis? *Radiology* 2003; 229(2):483–491.
- Goldman LW. Principles of CT: radiation dose and image quality. *J Nucl Med Technol* 2007; 35:213–225.
- American Association of Physicists in Medicine. The measurement, reporting, and management of radiation dose in CT; 2008. Available at: http://www.aapm.org/pubs/reports/rpt_96.pdf. Accessed January 15, 2012.
- Marin D, Nelson RC, Schindera ST, et al. Low-tube-voltage, high-tube-current multidetector abdominal CT: improved image quality and decreased radiation dose with adaptive statistical iterative reconstruction algorithm—initial clinical experience. *Radiology* 2010; 254:145–153.
- Yanagawa M, Honda O, Yoshida S, et al. Adaptive statistical iterative reconstruction technique for pulmonary CT: image quality of the cadaveric lung on standard- and reduced-dose CT. *Acad Radiol* 2010; 17:1259–1266.
- Hara AK, Paden RG, Silva AC, et al. Iterative reconstruction technique for reducing body radiation dose at CT: feasibility study. *AJR Am J Roentgenol* 2009; 193:764–771.
- Yu Z, Thibault JB, Bouman CA, et al. Fast model-based X-ray CT reconstruction using spatially nonhomogeneous ICD optimization. *IEEE Trans Image Process* 2011; 20:161–175.
- Wall BF, Hart D. Revised radiation doses for typical X-ray examinations. Report on a recent review of doses to patients from medical X-ray examinations in the UK by NRPB. National Radiological Protection Board. *Br J Radiol* 1997; 70:437–439.

Prognostic Importance of Volumetric Measurements in Stage I Lung Adenocarcinoma¹

Masahiro Yanagawa, MD, PhD
 Yuko Tanaka, MD
 Ann N. Leung, MD
 Eiichi Morii, MD, PhD
 Masahiko Kusumoto, MD, PhD
 Shunichi Watanabe, MD, PhD
 Hirokazu Watanabe, MD, PhD
 Masayoshi Inoue, MD, PhD
 Meinoshin Okumura, MD, PhD
 Tomoko Gyobu, MD
 Ken Ueda, MD
 Osamu Honda, MD, PhD
 Hiromitsu Sumikawa, MD, PhD
 Takeshi Johkoh, MD, PhD
 Noriyuki Tomiyama, MD, PhD

¹From the Department of Diagnostic Radiology, Stanford University School of Medicine, 1201 Welch Rd, Stanford, CA 94305 (M.Y., A.N.L.); Departments of Radiology (M.Y., T.G., K.U., O.H., H.S., N.T.), Pathology (E.M.), and Respiratory Surgery (S.W.), Osaka University Graduate School of Medicine, Suita, Osaka, Japan; Department of Radiology, Fujieda Municipal General Hospital, Fujieda, Shizuoka, Japan (E.M.); Department of Radiology (M.K., H.W.) and Division of Thoracic Surgery (M.I., M.O.), National Cancer Center, Tokyo, Japan; and Department of Radiology, Kinki Central Hospital of Mutual Aid Association of Public School Teachers, Itami, Hyogo, Japan (T.J.). Received August 13, 2013; revision requested September 16; revision received October 26; accepted December 10; final version accepted January 9, 2014. Address correspondence to M.Y. (e-mail: m-yanagawa@radiol.med.osaka-u.ac.jp).

© RSNA, 2014

Purpose:

To perform volumetric analysis of stage I lung adenocarcinomas by using an automated computer program and to determine value of volumetric computed tomographic (CT) measurements associated with prognostic factors and outcome.

Materials and Methods:-

Consecutive patients ($n = 145$) with stage I lung adenocarcinoma who underwent surgery after preoperative chest CT were enrolled. By using volumetric automated computer-assisted analytic program, nodules were classified into three subgroups: pure ground glass, part solid, or solid. Total tumor volume, solid tumor volume, and percentage of solid volume of each cancer were calculated after eliminating vessel components. One radiologist measured the longest diameter of the solid tumor component and of total tumor with their ratio, which was defined as solid proportion. The value of these quantitative data by examining associations with pathologic prognostic factors and outcome measures (disease-free survival and overall survival) were analyzed with logistic regression and Cox proportional hazards regression models, respectively. Significant parameters identified at univariate analysis were included in the multiple analyses.

Results:

All 22 recurrences occurred in patients with nodules classified as part solid or solid. Multiple logistic regression analysis revealed that percentage of solid volume of 63% or greater was an independent indicator associated with pleural invasion ($P = .01$). Multiple Cox proportional hazards regression analysis revealed that percentage of solid volume of 63% or greater was a significant indicator of lower disease-free survival (hazard ratio, 18.45 [95% confidence interval: 4.34, 78.49]; $P < .001$). Both solid tumor volume of 1.5 cm³ or greater and percentage of solid volume of 63% or greater were significant indicators of decreased overall survival (hazard ratio, 5.92 and 9.60, respectively [95% confidence interval: 1.17, 30.33 and 1.17, 78.91, respectively]; $P = .034$ and $.036$, respectively).

Conclusion:

Two volumetric measurements (solid volume, ≥ 1.5 cm³; percentage of solid volume, $\geq 63\%$) were found to be independent indicators associated with increased likelihood of recurrence and/or death in patients with stage I adenocarcinoma.

© RSNA, 2014

Adenocarcinoma is the most common subtype of lung cancer. In 2011, a new classification of adenocarcinoma (1) was developed to standardize diagnostic criteria and terminology applied to the wide spectrum of entities encompassed in this histologic subtype, which can range from indolent to lethal tumors. Results from several studies (2–5) have shown by using computed tomographic (CT) imaging that morphologic structure of adenocarcinoma can be predictive of tumor grade and patient prognosis. As emphasized in the recently published recommendations for subsolid nodules from the Fleischner Society (6), measurement of solid components and determination of the relative percentages of solid versus ground-glass portions of subsolid nodules are important because an increase in the extent of a solid component is associated with a higher likelihood of an invasive tumor. However, integration of this type of prognostic CT data into clinical management algorithms for adenocarcinoma has been relatively hindered by the lack of standardized methods for tumor characterization and measurement, particularly in the setting of part-solid nodules.

Volumetric measurement of nodules is a promising technique that has been shown (7–11) to be both accurate and precise for the quantification of small solid nodules. However, volumetric assessment of subsolid nodules is more challenging because of difficulties in segmentation and accurate

delineation between a tumor's ground-glass margins and the adjacent normal parenchyma. By using manual measurements, de Hoop et al (12) compared diameter, volume, and mass (volume \times CT value) of 52 ground-glass nodules (GGNs) that were followed as part of a lung cancer screening trial; among the three measures, they found that mass of GGN was subject to less variability and allowed earliest detection of growth in malignant nodules. Ko et al (11) reported similar growth-related results in five solid and three subsolid malignant nodules that were detected earlier with volumetric measurements obtained by using a semiautomated computer algorithm than with radiologic criteria used in current practice.

We hypothesized that volumetric measurement of solid and nonsolid components of early-stage adenocarcinoma seen by using CT imaging can provide prognostic information. The purpose of our study was to perform volumetric analysis of stage I lung adenocarcinomas by using an automated computer program and to determine the value of volumetric CT measurements associated with prognostic factors and patient outcome.

Materials and Methods

Patients

We obtained approval from our internal institutional review board; informed consent was waived for retrospective review of patient records and images. The study population consisted of 145 consecutive patients (68 men and 77 women; mean age, 63.6 years \pm 9.6 [standard deviation]; range, 31–82 years) who had undergone lobectomy ($n = 104$) or segmentectomy ($n = 41$) for pathologic stage I adenocarcinoma

Implication for Patient Care

- Automated volumetric analysis of early-stage adenocarcinomas can be associated with prognosis and may be helpful in determining appropriate treatment of patients with subsolid nodules.



at our hospital from April 1999 to April 2006 and had a preoperative thin-section chest CT study available for review. All patients were node-negative based on fluorine 18 fluorodeoxyglucose (FDG) positron emission tomographic (PET) staging study. Hilar and mediastinal lymph node resections were performed in 104 patients with lobectomy, and hilar lymph nodal sampling was performed in 41 patients with segmentectomy at the time of tumor resection. Individuals who had history of adenocarcinoma of the lung or other organs or who had received induction chemotherapy before surgery were excluded from the study.

After hospital discharge, all patients were evaluated at 3-month intervals. The evaluation included a physical examination, chest x-ray, and blood tests (including tumor markers). Additional thoracoabdominal CT scans were generally obtained at 6-month intervals. Recurrence was confirmed at CT and, if necessary, FDG PET imaging. The median follow-up period of all 145 patients after surgery was 6.2 years (range, 0.86–12.63 years). Complete follow-up information until death or January 2013 was available for all patients. During the follow-up period, 22 patients experienced disease recurrence with seven associated cancer-related deaths.

Advances in Knowledge

- Automated volumetric analysis of stage I adenocarcinoma allowed quantification of CT features associated with patient outcome.
- Radiologist and software classification of nodules into subsolid and solid subtypes showed excellent agreement ($\kappa = 0.81$).
- Volumetric measurements of tumor solid component and percentage of solid volume were associated with recurrence and/or death, whereas measurement of total tumor volume was not.

Published online before print

10.1148/radiol.14131903 Content codes:  

Radiology 2014; 272:557–567

Abbreviations:

FDG = fluorine 18 fluorodeoxyglucose

FWHM = full width at half maximum

GGN = ground-glass nodule

Author contributions:

Guarantors of integrity of entire study, M.Y., Y.T., S.W., H.W., T.G., K.U., O.H.; study concepts/study design or data acquisition or data analysis/interpretation, all authors; manuscript drafting or manuscript revision for important intellectual content, all authors; approval of final version of submitted manuscript, all authors; literature research, M.Y., Y.T., A.N.L., E.M., K.U., T.J.; clinical studies, M.Y., Y.T., E.M., M.K., S.W., H.W., M.I., M.O., O.H., H.S., T.J.; experimental studies, M.Y., Y.T., E.M., T.G., H.S., T.J.; statistical analysis, M.Y., A.N.L., E.M., M.K., S.W., H.W.; and manuscript editing, M.Y., A.N.L., E.M., O.H., T.J., N.T.

Conflicts of interest are listed at the end of this article.

Scanning Protocols

Chest CT scans were acquired by using a four-detector row CT scanner (LightSpeed QXi; GE Healthcare, Milwaukee, Wis) and an eight-detector row CT scanner (LightSpeed Ultra; GE Healthcare). Acquisition parameters were as follows: collimation, 0.625 mm or 1.25 mm; pitch, 0.625–1.5; rotation time, 0.4–0.8 seconds per rotation; exposure parameters, 120 kV and 200 mA; field of view, 200 mm. All image data were reconstructed with a high spatial frequency algorithm at contiguous section thicknesses of 0.625 mm or 1.25 mm.

Visual Analysis

CT scans were displayed on a monitor at lung window settings (level, -700 HU; width, 1200 HU). Two independent chest radiologists (G.T. and H.S., with 9 and 13 years of experience, respectively) visually classified tumors into three subgroups: pure GGN, part-solid GGN, and solid. GGN was defined as an area that exhibited a slight, homogeneous increase in density, which did not obscure underlying vascular markings. Solid was defined as an area of increased opacity that completely obscured underlying vascular markings. The two radiologists designated the distribution of each nodule as peripheral (outer one-third of lung, but not in contact with pleura), middle (inner two-thirds of lung), or juxtapleural (in contact with pleura). Final evaluations were decided by a consensus panel, which consisted of the same two radiologists and an adjudicator (O.H., with 21 years of experience in chest radiologic imaging), as needed. By using electronic calipers, one chest radiologist (M.Y., with 12 years of experience) measured the longest diameter of the solid component and of total tumor; solid proportion was defined as the ratio of the longest diameter of the solid component divided by the longest diameter of total tumor multiplied by 100%.

Computer Analysis

We developed our software by using commercial software (Microsoft Visual C++ 6.0; Microsoft, Redmond, Wash) on a commercially available personal

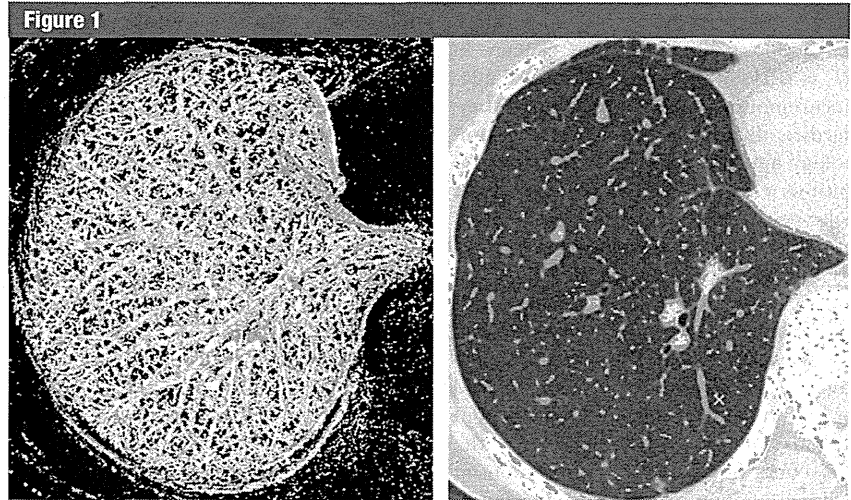


Figure 1: Images show extraction of vessels by using a multiscale three-dimensional line filter. (a) Volume rendering image of all vessels identified by the three-dimensional line filter. (b) Green areas in right lung correspond to extracted vessels.

computer. Incorporated in our software is a previously described (13) three-dimensional line filter that enabled the enhancement of curvilinear structures, such as vessels, in three-dimensional medical images on the basis of a combination of the eigenvalues of the three-dimensional Hessian matrix. Multiscale integration is formulated by taking the maximum among single scale filter responses, and its characteristics are examined to derive criteria for the selection of parameters in the formulation. The resultant multiscale line-filtered images provide improved segmentation and visualization of curvilinear structures. This three-dimensional line filter was used as the first step to eliminate vessels on the CT images (Fig 1). Quantitative analysis was then performed by one observer (M.Y., 12 years of experience in chest radiology) who was required to place an over-inclusive region of interest around each nodule after selecting a tumor center point (ie, a seed point) (Fig 2). The threshold value on CT between a tumor and surrounding normal lung parenchyma was automatically determined by applying CT density profile curves, one-dimensional quantitative CT values across the nodule, through the seed point at 10° intervals on each axial section

(14) (Fig 3a). A CT value that corresponded to full width at half maximum (FWHM) was measured from each profile curve, and the mean FWHM from the 36 density profiles was used as threshold value (Fig 3b). FWHM is a mathematically well-defined parameter used to describe a measurement of the width of an object in imaging when that object does not have sharp edges. The width of the CT density profile curve is often decided by the FWHM (15,16). Following this approach, we used the CT value that corresponded to mean FWHM as an objective, standardized method to determine the threshold CT value between the tumor and surrounding normal lung parenchyma.

The tumor was also segmented by using a three-dimensional region-growing algorithm (17) that, after placement of an initial seed point, added in neighboring pixels with attenuation values above defined threshold value that did not contain vessels. The volume of the tumor was calculated as follows: (number of voxels within segmented region) \times unit volume. Unit volume was defined as the product of x-, y-, and z-axes in a raw image.

On the basis of a previously reported threshold selection and nodule classification method (18), we used

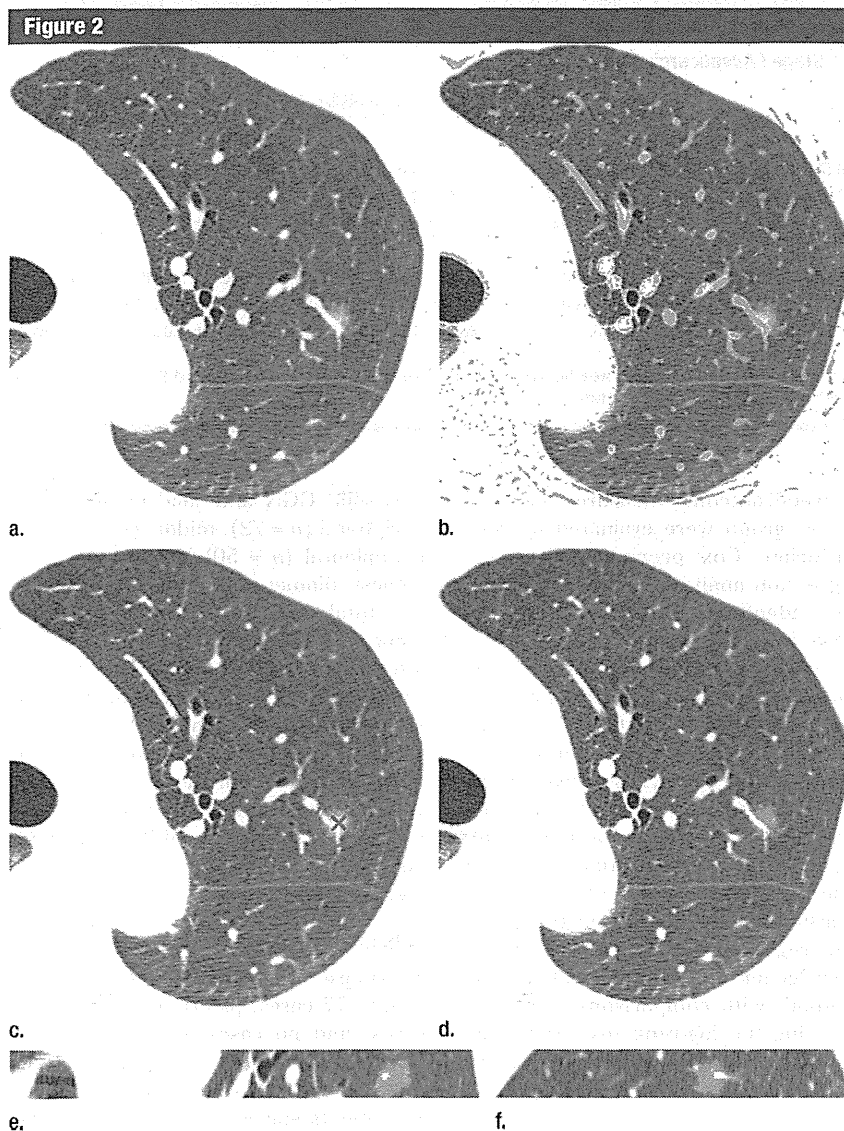


Figure 2: Images show sequential steps in volumetric analysis of a pure GGN in a 57-year-old woman. (a) Thin-section CT image shows a pulmonary vein traversing an 8.1-mm GGN in the left upper lobe. (b) Three-dimensional line filter identifies and extracts vessels (green areas). (c) An over-inclusive region of interest is drawn manually around the nodule in red. (d) Axial image, (e) coronal image, and (f) sagittal image of GGN. Nodule is automatically segmented (shown as highlighted green area) with calculation of GGN and solid components. Total volume, solid volume, and percentage of solid volume for this nodule are 0.14 cm³, 0.00 cm³, and 0.00%, respectively.

−291 HU as the threshold CT value between ground glass and solid. By using this value, each voxel of ground glass and solid included in a segmented tumor was automatically determined; total tumor volume, solid volume, and percentage of solid volume (solid volume/tumor

volume × 100%) were calculated; and the nodule was classified into three subgroups (pure GGN [$>98\%$ of tumor with attenuation of −291 HU or less], part-solid GGN [2%–71.5% of tumor with attenuation greater than −291 HU], and solid [$>71.5\%$ of tumor with

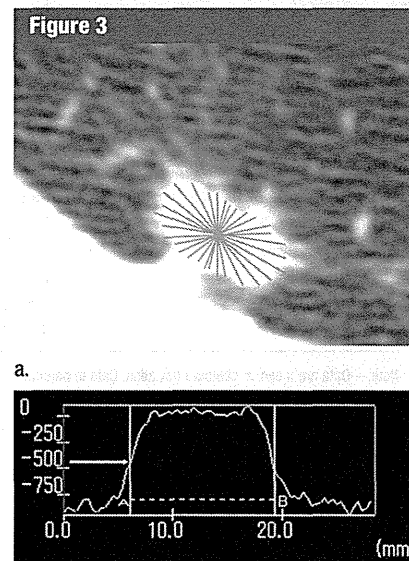


Figure 3: Threshold CT value between a tumor and surrounding normal lung parenchyma in a 60-year-old woman. (a) CT density profile curves are drawn through center of nodule at 10° intervals. (b) A representative profile curve shows CT value at FWHM is −545 HU (arrow). The mean CT value derived from all 36 profile curves on each axial section is used as the threshold CT value.

attenuation greater than −291 HU] (18). Before beginning this study, we performed computer-assisted analysis of 10 nodules that were not included in this study that by qualitative evaluation consisted of pure ground-glass attenuation. In these 10 cases, percentage of solid volume ranged from 0% to 1.9% (mean, 0.8% ± 1.1% [standard deviation]); therefore, percentage of solid volume in the GGN subgroup was defined as less than 2%.

Pathologic Analysis

The presence of lymphatic, vascular, and pleural invasion was evaluated by two pathologists. Final evaluation was decided in consensus. Immunostaining methods by using D2-40 (Covance, San Diego, Calif), a lymphatic-specific monoclonal antibody, and CD31 (Dako, Glostrup, Denmark), an endothelial antigen, were performed to optimize identification of lymphatic and vascular channels, respectively (19,20).

Table 1

Quantitative Measurements in 145 Patients with Stage I Adenocarcinoma

Parameter	All Patients	Patients with Pure GGN	Patients with Part-Solid GGN	Patients with Solid Tumor
Visual analysis				
Longest diameter of tumor (mm)	15.7 ± 4.8 (7.0–31.0)	11.2 ± 2.7 (7.0–14.9)	15.9 ± 4.6 (7.2–31.0)	16.9 ± 5.1 (7.0–31.0)
Longest diameter of solid component (mm)	9.6 ± 7.0 (0.0–31.0)	0.0 ± 0.0 (0.0–0.0)	7.5 ± 4.7 (1.0–21.0)	16.9 ± 5.1 (7.0–31.0)
Solid proportion (%)	58.3 ± 37.1 (0.0–100.0)	0.0 ± 0.0 (0.0–0.0)	47.2 ± 26.5 (11.4–95.0)	100.0 ± 0.0 (100.0–100.0)
Computer analysis				
Tumor volume (cm ³)	2.46 ± 2.87 (0.03–16.97)	0.64 ± 0.54 (0.03–1.62)	1.92 ± 2.23 (0.05–15.60)	4.01 ± 3.58 (0.45–16.97)
Solid volume (cm ³)	1.47 ± 2.18 (0.00–14.28)	0.00 ± 0.02 (0.00–0.12)	0.75 ± 0.82 (0.003–4.09)	3.22 ± 3.00 (0.35–14.28)
Solid volume (%)	49.1 ± 28.2 (0.00–90.40)	0.21 ± 0.5 (0.00–1.90)	40.9 ± 19.9 (6.30–71.50)	78.7 ± 5.0 (71.60–90.40)

Note.—Data are mean ± standard deviation. Data in parentheses are range. For group classification, there were 145 patients total, 15 with pure GGN, 83 with part-solid GGN, and 47 with solid tumor. For visual analysis, there were 145 patients total, 15 with pure GGN, 86 with part-solid GGN, and 44 with solid tumor.

Statistical Analysis

We evaluated the value of eight features of CT (visual classification, software classification, longest diameter of solid component, longest diameter of total tumor, solid proportion, total tumor volume, solid volume, and percentage of solid volume) to examine associations with three prognostic factors (lymphatic invasion, vascular invasion, and pleural invasion) and two outcome measures (overall survival and disease-free survival). All statistical analyses were performed by using commercially available software (MedCalc version 8.0.0.1; Frank Schoonjans, Mariakerke, Belgium). Agreement between visual and software classification of nodule subgroups was evaluated by using the κ statistic, and it was classified as poor ($\kappa = 0.00$ – 0.20), fair ($\kappa = 0.21$ – 0.40), moderate ($\kappa = 0.41$ – 0.60), good ($\kappa = 0.61$ – 0.80), or excellent ($\kappa = 0.81$ – 1.00) (21). For each CT feature, the cutoff value that yielded the largest difference in numbers of patients with and without recurrence and death was determined by using the empirical receiver operating characteristic method. Receiver operating characteristic analyses were all univariate. The optimal thresholds were determined for each variable separately. Subsequently, associations between prognostic factors and each binary group designated by the cutoff value for the eight CT features were evaluated by using univariate logistic regression analysis. Similarly, associations

between outcome measures and each binary group were evaluated by using univariate Cox proportional hazards regression analysis. Significant parameters identified by univariate analysis were included in the multiple logistic regression and Cox proportional hazards regression models (stepwise method; P value of .05 or less was used for entry into the model and P value greater than .1 was selected for removal), respectively. The 123 patients (85.0%) with no observed failure events in the present study were considered censored for the two outcome measures in the Cox proportional hazards regression model. Survival curves were generated by the Kaplan-Meier method, with comparisons performed by using the log-rank test. A P value of less than .05 indicated statistical significance.

Results

Visual and Computer Analyses

Results of all 145 patients are summarized in Table 1. Classification of nodules (per two radiologists) into pure GGN, part-solid GGN, and solid subtypes showed excellent agreement ($\kappa = 0.90$). There was excellent agreement ($\kappa = 0.81$) between visual and computer classification of nodule subgroups with disagreements on only five nodules.

Distribution of pure GGN was peripheral ($n = 12$), middle ($n = 2$), and juxtaleural ($n = 1$); distribution of

part-solid GGN and solid nodules was peripheral ($n = 72$), middle ($n = 8$), and juxtaleural ($n = 50$). Mean measured longest diameter of solid component and total tumor were $9.6 \text{ mm} \pm 7.0$ (range, 0–31.0 mm) and $15.7 \text{ mm} \pm 4.8$ (range, 7.0–31.0 mm), respectively. Calculated solid proportion of nodules was 58.3%–37.1% (range, 0%–100%). Total tumor volume, solid volume, and percentage solid volume were $2.46 \text{ cm}^3 \pm 2.87$ (range, 0.033–16.97 cm^3), $1.47 \text{ cm}^3 \pm 2.18$ (range, 0–14.28 cm^3), and $49.1\% \pm 28.2$ (range, 0%–90.4%), respectively.

Pathologic Analysis

There were identified lymphatic invasion in 17 cases, pleural invasion in 13 cases, and no cases of vascular invasion. There were 118 patients staged as pT1a, 14 patients staged as pT1b, and 13 patients staged as pT2. No patients were found to have lymph node metastases. According to pathologic analysis, there were 132 patients staged as Ia and 13 patients staged as Ib.

Relationship with Prognostic Factors

On the basis of receiver operating characteristic analysis, both visually and computer-classified subgroups were re-sorted into pure GGN and solid (part-solid GGN and solid) divisions. Cutoff values for the six CT features were as follows: longest diameter of solid component, 9.9 mm; longest tumor diameter, 18 mm; solid proportion, 78%; total tumor volume,